PAPER

Check for updates

Extrinsic pseudocapacitive ultrathin 2D MoS$_2$ nanoflakes clamped on 1D Sb$_2$S$_3$ nanorods: an advanced heterostructured anode for high-energy ammonium ion hybrid capacitors†

Supriya J. Marje,[a] Harshitha B. Tyagaraj,[a] Seung-Kyu Hwang,[b]
Kugalur Shanmugam Ranjith,[a] Ebrahim Alhajri,[c] Nilesh R. Chodankar, [ID] *[c]
Yun Suk Huh [ID] *[b] and Young-Kyu Han [ID] *[a]

Ammonium-ion (NH$_4^+$) charge carriers have recently been considered promising for electrochemical energy storage (EES) systems because of their high safety, low molar mass, and small hydrated radius (3.31 Å). However, finding a kinetically balanced anode and cathode combination for high NH$_4^+$-ion storage is challenging. Herein, a new approach for developing a heterostructured electrode was developed by constructing extrinsic pseudocapacitive 2D ultrathin MoS$_2$ nanoflakes clamped on 1D Sb$_2$S$_3$ nanorods (MoS$_2$/Sb$_2$S$_3$) as an anode for high-performance ammonium-ion hybrid capacitors (AIHCs) against the intrinsic pseudocapacitive MnO$_2$ cathode. The engineered MoS$_2$/Sb$_2$S$_3$ heterostructured anode facilitated large interlayer galleries owing to the presence of 2D MoS$_2$ for facial NH$_4^+$-ion diffusion and provided a rapid electron pathway through 1D Sb$_2$S$_3$, which promoted a high capacitance of 360 F g^{-1}, low resistance, and stable cycling performance. More importantly, the constructed AIHC delivered a superior energy density of 43.75 W h kg^{-1} at a power density of 600 W kg^{-1} and excellent cycling durability over 5000 cycles. These results show that a heterostructured extrinsic pseudocapacitive anode can improve the electrochemical parameters of NH$_4^+$ EES systems and replace traditional carbon-based anode materials.

Introduction

The demand for green energy continues to inspire the world-wide research community to research and develop next-generation storage systems.[1] Rechargeable batteries play a crucial role in electric vehicles, portable devices, and grid-scale storage applications.[2] As current batteries tend to use organic electrolytes, which have safety issues along with toxicity and flammability,[3] the use of aqueous electrolytes is desired owing to their inherent merits, such as low cost, high ionic conductivity, environmental friendliness, and non-flammability. Moreover, their flexibility in formation and

manufacturing make them attractive in the battery industry.[4,5] Therefore, aqueous batteries are the focus of research interest and are considered future substitutes for commercial secondary batteries.[6,7] Aqueous batteries usually contain metallic cations, such as Li$^+$, Zn^{2+}, Na$^+$, Mg^{2+}, K$^+$ or Al^{3+}, which act as charge carriers. However, their large hydration volumes and high molar masses hamper the diffusion kinetics of these ions and result in poor rate capability and stability.[8] In contrast, non-metallic ions have smaller hydration radii, low molar masses, and high availability. Furthermore, these features result in low costs, high energy densities, and excellent rate capabilities.[9,10] In this context, non-metal cation carriers, such as protons,[11] hydronium,[12] and NH$_4^+$ ions, have exceptional features.[13] In particular, the highly conductive nature of the NH$_4^+$ ion makes it an efficient charge carrier, which promotes ion-diffusion processes, and it also has a lower HER (hydrogen evolution reaction) potential and is less corrosive.[8,14] Furthermore, NH$_4^+$ ions can migrate rapidly because of their smaller Stokes radius and energy barriers and tetrahedral geometries, which support their superior intercalation in host materials.[15,16]

Relatively few studies have been reported on ammonium-ion storage and those that have been reported mainly focused on cathode materials for ammonium-ion storage. It was found that

[a]Department of Energy and Material Engineering, Dongguk University-Seoul, Seoul, 04620, South Korea. E-mail: ykenergy@dongguk.edu

[b]NanoBio High-Tech Materials Research Center, Department of Biological Sciences and Bioengineering, Inha University, Incheon, 22212, South Korea. E-mail: yunsuk.huh@inha.ac.kr

[c]Mechanical Engineering Department, Khalifa University, Abu Dhabi, 127788, United Arab Emirates. E-mail: chodankarnilesh311@gmail.com

† Electronic supplementary information (ESI) available: Details of materials synthesis, characterization, and electrochemical measurements, additional XRD, XPS, SEM, TEM, and electrochemical performance. See DOI: https://doi.org/10.1039/d4ta00262h.

This journal is © The Royal Society of Chemistry 2024

J. Mater. Chem. A, 2024, 12, 7587–7597 | 7587

the exceptional features of cathode materials improve the capacity and cycling stability of devices.[16] Several cathode materials have been explored for ammonium-ion storage, such as activated carbon cloth (ACC)@V_2O_5,[15] MnAl LDH,[9] MnO_2,[17–20] and Prussian blue (NiHCF).[21] However, little work has been published on high-performance anode materials for ammonium-ion storage, yet the development of such materials is crucial. Generally, a suitable material must meet specific parameters; for example, it should have an appropriate electrode structure and bonding sites. A suitable space and binding sites are required for the accommodation and binding of NH_4^+ ions during the reaction.[22] The primary mechanism underlying rapid NH_4^+ storage involves the formation and breaking of hydrogen bonds.[23,24] However, researchers face challenges with the structural collapse of the host material due to the frequent insertion/extraction of NH_4^+.[21] Therefore, novel electrodes for NH_4^+-storage systems are still required to enhance the performance and long-term stability of ammonium-ion capacitors.

Traditionally, carbon-based materials have been used as anodes due to their excellent electrochemical cycling stability.[25–28] However, the double-layer charge storage limits the capacitance of carbon anodes and causes a large kinetic imbalance between anode and cathode materials. This can negatively affect the capacitance and energy density of cells, as indicated by the equation $1/C_T = 1/C_1 + 1/C_2$,[29] where C_T, C_1, and C_2 are the capacitances of the whole cell, cathode and anode electrodes, respectively.[30] For this reason, it is crucial to find anode materials with energy-storage capacities similar to cathode materials to assemble kinetically balanced ammonium-ion energy-storage systems.[31,32] Considering these issues, redox-active anode materials that can simultaneously provide high capacitance and stability at negative operating potentials are needed.[31–34] Of the many potential candidates, extrinsic pseudocapacitive metal sulfides are promising for aqueous ion capacitors because of their exceptional electrochemical properties and structural diversities.[33,35,36] Specifically, because of its structural stability, Sb_2S_3 was investigated for electrocatalysis, battery and photovoltaic device applications. In addition, Sb_2S_3 has the merits of being nontoxic, abundant in nature, and cheap.[37] However, the volume expansion of Sb_2S_3 during the intercalation/deintercalation of ions hampers its stability and rate performance; though this issue can be managed by fabricating sulfide-based heterostructures that can maintain their structures.[38] Correspondingly, nanostructures covered with a protective layer provide space for volume changes, stabilize the electrode/electrolyte interfaces, and promote electron transport with shorter ion-diffusion paths.[39,40]

Thus, we were motivated to develop anode materials that would enhance the electrochemical performance of NH_4^+-storage systems. Consequently, we investigated heterostructured metal chalcogenide-based anode materials for ammonium-ion hybrid capacitors (AIHCs) using a straightforward solution path. Nanorods of Sb_2S_3 served as a 1D conductive core, while 2D MoS_2 nanosheets offered abundant active sites with large interlayer galleries that could promote facial ion movement during charge–discharge processes. The engineered heterostructured Sb_2S_3/MoS_2 anode delivered a specific capacitance of 360 F g^{-1} (at 3 A g^{-1}) and excellent cycling performance (5000 cycles at 12 A g^{-1}) within a negative potential window (−0.75 to 0.05 V/SCE) in ammonium-ion electrolyte. Furthermore, an AIHC fabricated by integrating MnO_2 as the cathode and Sb_2S_3/MoS_2 as the anode exhibited excellent a high energy density and stability, which represented a substantial improvement over previously reported carbon-anode containing AIHCs.[15,20]

Experimental section

Synthesis of Sb_2S_3

Analytical-grade chemicals and reagents were used without further purification. Sb_2S_3 nanorods were synthesized using a hydrothermal method. For a typical synthesis, $SbCl_3$ (3 mmol), L-cysteine (6 mmol), and $Na_2S \cdot 9H_2O$ (6 mmol) were dissolved in 40 ml of double distilled water (DDW) with stirring. The solution was then transferred to a 50 ml Teflon-lined stainless-steel autoclave and heated for 12 h at 180 °C. A dark-brown precipitate of Sb_2S_3 was obtained after cooling to room temperature. The product was collected after filtration, washed with DDW several times, and dried at 60 °C overnight.

Synthesis of Sb_2S_3/MoS_2

To synthesize Sb_2S_3/MoS_2, 50 mg of Sb_2S_3 was suspended in 40 ml of DDW containing $(NH_4)_6Mo_7O_{24}$ (0.01 mol) and thiourea (0.02 mol), stirred, and sonicated for 30 min. The prepared solution was transferred to a 50 ml Teflon-lined stainless-steel autoclave and heated for 24 h at 200 °C. The final product was obtained by suspending it several times sequentially in DDW and ethanol and centrifuging between steps. The obtained Sb_2S_3/MoS_2 was dried overnight at 60 °C.

Synthesis of MnO_2

MnO_2 films were electrodeposited on carbon cloth (CC) using an equimolar $MnSO_4$ (0.1 mol) and Na_2SO_4 (0.1 mol) solution and an electrochemical workstation. The potential was varied from 0.4–1.5 V at a scan rate of 50 mV s^{-1} in potentiodynamic mode for 50, 100, 150, or 200 cycles, and the samples produced were denoted as Mn-50, Mn-100, Mn-150, and Mn-200, respectively. In a three-electrode cell, the CC, graphite, and saturated calomel electrodes (SCE) were used as the working, counter, and reference electrodes. The as-deposited MnO_2 films were dried overnight at 60 °C.

Results and discussion

A two-step hydrothermal process was employed to synthesize heterostructured Sb_2S_3/MoS_2 (Fig. 1a). A simple hydrothermal method was first used to synthesize Sb_2S_3 nanorods. In this process, $SbCl_3$ and L-cysteine served as the sources of Sb^{3+} and S^{2-}, respectively. This step was followed by a hydrothermal step to grow MoS_2 nanosheets on the surfaces of Sb_2S_3 nanorods using $(NH_4)_6Mo_7O_{24}$ and thiourea as the sources of Mo^{4+} and S^{2-}, respectively. It is known that the self-aggregation and disordered arrangement of a material can restrict exposure of
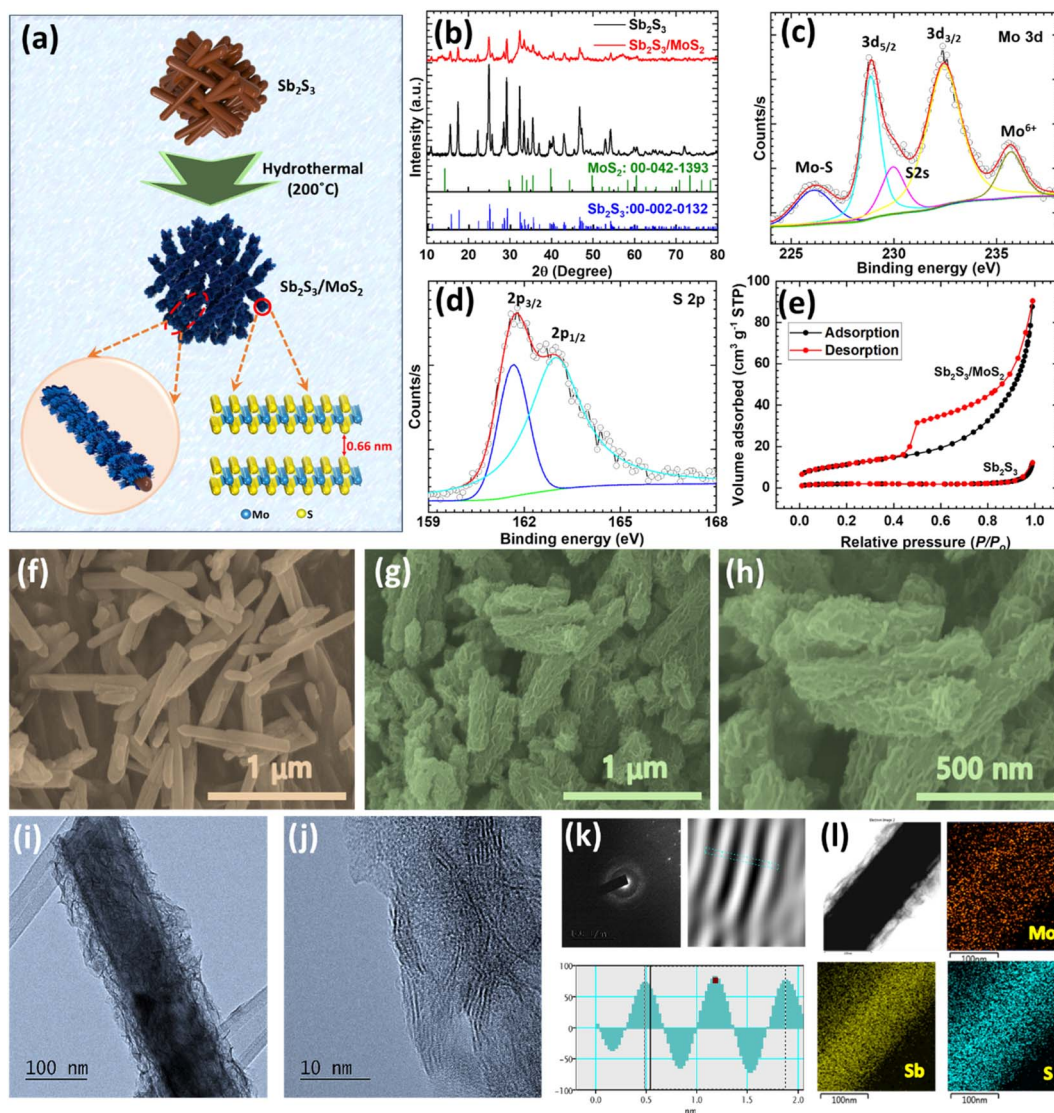
7588 | J. Mater. Chem. A, 2024, 12, 7587–7597

This journal is © The Royal Society of Chemistry 2024

Fig. 1 (a) Schematic of the two-step hydrothermal synthesis process used to produce heterostructured Sb_2S_3/MoS_2. (b) XRD patterns of Sb_2S_3 and Sb_2S_3/MoS_2. High-resolution XPS spectra of (c) Mo 3d and (d) S 2p. (e) N_2 adsorption–desorption isotherms of Sb_2S_3 and Sb_2S_3/MoS_2. SEM images of (f) Sb_2S_3 and (g and h) Sb_2S_3/MoS_2. (i–l) TEM images and elemental mapping of Sb_2S_3/MoS_2.

the active sites,[41] which can result in a lower redox reaction kinetics and lower specific capacitance. So, it is important to expose an optimum amount of functional material through finely tuning and engineering a suitable architecture to meet definite requirements.[42] To load the optimum amount and achieve the required architecture of MoS_2 on Sb_2S_3 nanorods, and also to prevent self-aggregation and a disordered arrangement of MoS_2 nanosheets on Sb_2S_3 nanorods, a second hydrothermal reaction was carried out using different deposition times. Scanning electron microscopy (SEM) analysis showed that the reaction for 24 h obtained good results, and thus, this time was adopted for the further study. The phases and crystallinities of the developed materials were investigated by X-ray diffraction (XRD) analysis. The diffraction peaks of Sb_2S_3 were well indexed with the orthorhombic phase of Sb_2S_3 (JCPDS 42-1393), indicating the successful formation of Sb_2S_3 (Fig. 1b).

The low crystallinity and small crystallite size of the as-produced MoS_2 were evidenced by the broad diffraction peaks (Fig. S1†). The XRD pattern of Sb_2S_3/MoS_2 was compatible with that of Sb_2S_3; no extra MoS_2 peaks were detected due to its low crystallinity (Fig. 1b).[43] The XRD study confirmed that MoS_2 nanosheets grew on Sb_2S_3, and the reduction in the intensities of the Sb_2S_3/MoS_2 diffraction peaks confirmed that MoS_2 nanosheets were uniformly decorated on Sb_2S_3 nanorods. The second hydrothermal step thus produced the required heterostructured Sb_2S_3/MoS_2 material.

X-Ray photoelectron spectroscopy (XPS) was utilized to characterize the chemical states and composition of the heterostructured Sb_2S_3/MoS_2. The wide-scan XPS survey spectrum confirmed the presence of Mo, Sb, S, and O (Fig. S2a†). In addition, high-resolution spectra was used to gain insights into the valence states. The Sb 3d spectrum (Fig. S2b†) was

deconvoluted into two peaks at 530.5 and 539.7 eV, associated with the Sb $3d_{5/2}$ and $3d_{3/2}$ of metallic Sb, respectively.[44] Besides, another peak was observed at 531.6 eV, which belonged to O 1s (Fig. S2c†), representing surface oxidation.[38,39] As depicted in Fig. 1d and e, the high-resolution XPS spectra of molybdenum and sulfur elements were investigated to determine the status of Mo 3d and S 2p. The peaks observed at 232.4 and 228.8 eV were ascribed to the Mo $3d_{3/2}$ and Mo $3d_{5/2}$ of Mo^{4+} (Fig. 1c).[45,46] The peak at 235.7 eV was related to Mo(vı), which reflected a partial reduction of the Mo surface (Mo–O). In this study, $(NH_4)_6Mo_7O_{24}$ was used as the source of molybdenum to synthesize MoS_2. During the 200 °C hydrothermal process, this material thermally decomposed into MoO_x, which accelerated the oxidation of Mo.[47] Another peak at 229.9 eV was observed corresponding to Mo(v), which may have resulted from the partial reduction of Mo^{6+}.[47] Furthermore, the peak that arose at around 226.1 eV was assigned to S 2s.[48] The S 2p spectrum displayed a S^{2-} doublet at 161.6 and 162.9 eV, attributed to S $3p_{3/2}$ and S $3p_{1/2}$ (Fig. 1d).[47,49] These XPS results were in accordance with previous studies on Mo, Sb, S, and O, and confirmed the successful formation of the Sb_2S_3/MoS_2 heterostructure with a Mo to S atomic ratio of 1 : 1.62. The specific surface areas of the prepared samples were determined using N_2 adsorption–desorption isotherm measurements. As presented in Fig. 1e, the Sb_2S_3/MoS_2 material displayed a type-III isotherm with an H3 type physisorption hysteresis loop according to the International Union of Pure and Applied Chemistry (IUPAC) classification, which is characteristic of mesoporous materials with a low adsorption energy. According to Brunauer–Emmett–Teller (BET) equation analysis, the surface area of the heterostructured Sb_2S_3/MoS_2 was 40.6 m^2 g^{-1}, which was seven times higher than that of Sb_2S_3 (5.8 m^2 g^{-1}). This large specific surface area of the heterostructured Sb_2S_3/MoS_2 suggests that it contains many more active sites than Sb_2S_3 and mesopores that shorten the diffusion path, which is desirable for rapid charge transfer.

SEM and transmission electron microscopy (TEM) were used to study the morphologies and structures of Sb_2S_3 and Sb_2S_3/MoS_2. The SEM images indicated that the Sb_2S_3 material had a rod-like structure and smooth surface (Fig. 1f), and a slightly porous surface was observed at higher magnification (Fig. S3a†). During the hydrothermal reaction, nanosheets of MoS_2 grew uniformly on the Sb_2S_3 nanorods (Fig. 1g and h), and the surface of Sb_2S_3 became rougher (Fig. S3b†). However, the nanorod-like structure of Sb_2S_3 was well maintained. The HR-TEM images of Sb_2S_3 revealed a rod-like structure with a smooth surface (Fig. S4a and b†) and a crystal lattice (d = 0.24 nm) assigned to the (240) plane of orthorhombic Sb_2S_3 (Fig. S4c and d†). The selected area electron diffraction (SAED) pattern of Sb_2S_3 revealed a highly regular crystal structure (Fig. S4e†). The uniform coating of MoS_2 nanosheets on Sb_2S_3 nanorods was clearly observed in the HR-TEM images of Sb_2S_3/MoS_2 (Fig. 1i), and the corrugated nanosheets showed a lattice fringe of 0.66 nm (Fig. 1j and k), consistent with the (002) plane of the MoS_2 material and sufficient to allow the quick intercalation/deintercalation of NH_4^+ ions. In addition, the SAED pattern of the corrugated nanosheets on Sb_2S_3/MoS_2 showed that the

MoS_2 nanosheets were largely amorphous (Fig. 1k). Additionally, energy dispersive X-ray (EDX) elemental mappings of the pristine Sb_2S_3 and heterostructured Sb_2S_3/MoS_2 material were measured, and disclosed the co-existence of Sb, S, and a small amount of O in the pristine Sb_2S_3 material (Fig. S4e† and 1l). The EDX mapping of Sb_2S_3/MoS_2 revealed Sb was uniformly distributed in the Sb_2S_3 core region, whereas Mo was less dense than Sb and was observed in the overall MoS_2 shell region. Likewise, uniform S distribution was also observed throughout the heterostructure Sb_2S_3/MoS_2 (Fig. 1l). The small amount of O observed in Sb_2S_3 and Sb_2S_3/MoS_2 confirmed the partial reduction of the material, which concurred with the XPS results (Fig. S4e, f and S5†). The uniform coverage of Mo and S on the core material confirmed the homogeneous growth of MoS_2 nanosheets on the Sb_2S_3 nanorods, which was consistent with the heterostructure of Sb_2S_3/MoS_2 observed by SEM and TEM analyses. The above investigation verified that MoS_2 nanosheets grew on the Sb_2S_3 nanorods, which aligned with the XRD and XPS results.

A series of tests were performed to evaluate the electrochemical properties of the developed Sb_2S_3/MoS_2 heterostructure for ammonium-ion storage. The ammonium-ion-storage performances of Sb_2S_3, MoS_2, and Sb_2S_3/MoS_2 electrodes were first measured in a half-cell system. Cyclic voltammetry (CV), galvanostatic charge–discharge (GCD), and electrochemical impedance spectroscopy (EIS) analyses of the active materials were performed in 1 M $(NH_4)_2SO_4$ electrolyte. The CV performances of Sb_2S_3, MoS_2, and Sb_2S_3/MoS_2 electrodes were measured in a similar potential range for comparison purposes in an optimized "−0.75 to 0.05 V (vs. SCE)" potential window (Fig. S6a†). The Sb_2S_3 electrode displayed oxidation and reduction peaks in the CV curves and delivered minimal capacitive performance due to its small CV area. In contrast, the MoS_2 electrode exhibited rectangular CV curves and a higher CV area than the Sb_2S_3 electrode. Interestingly, the Sb_2S_3/MoS_2 electrode exhibited a much higher current response and almost rectangular shape without any specific redox peaks, indicating the pseudocapacitive nature of the heterostructure due to the MoS_2 along with a higher capacity. The GCD profiles of the Sb_2S_3, MoS_2, and Sb_2S_3/MoS_2 electrodes are depicted in Fig. S6b† (at a current density of 10 A g^{-1}) and displayed the significantly distinguished storage behavior. Triangular symmetric curves were noted, without any voltage plateau, for the MoS_2 and Sb_2S_3/MoS_2 electrodes, confirming the pseudo-capacitive nature of the materials. The discharge time of Sb_2S_3/MoS_2 was much longer than that of Sb_2S_3 and MoS_2. Also, the potential window achieved by the Sb_2S_3/MoS_2 electrode was higher than that of the Sb_2S_3 electrode at the same current density (10 A g^{-1}). So, the calculated specific capacitance of the heterostructured Sb_2S_3/MoS_2 electrode (258.2 F g^{-1}) was 2.25-fold higher than that of the Sb_2S_3 (156.8 F g^{-1}) and MoS_2 (159.7 F g^{-1}) electrodes. The enhanced electrochemical performance for the Sb_2S_3/MoS_2 electrodes was due to: (1) the rapid electron transfer provided by the conductive core 1D Sb_2S_3, (2) the greater number of active sites provided by the MoS_2 host, and hence, greater specific surface area, (3) the huge number of active sites and increased redox activity provided by the 2D

7590 | J. Mater. Chem. A, 2024, 12, 7587–7597

This journal is © The Royal Society of Chemistry 2024

MoS_2 layer, and (4) the large MoS_2 interlayer distance allowing the rapid intercalation of NH_4^+ ions.

The comparative EIS spectra of the Sb_2S_3, MoS_2, and Sb_2S_3/MoS_2 electrodes were plotted and simulated based on an equivalent circuit, as shown in Fig. S6c.† Each electrode displayed a semicircle in the high-frequency region and a straight line in the low-frequency region. The semicircle was attributed to charge-transfer resistance (R_{ct}) and the straight line to diffusion resistance (W). The high-frequency interaction with the X-axis corresponded to solution resistance (R_s), which was related to the internal resistance of the electrode, electrolyte conductivity, and electrode/electrolyte contact resistance. In an equivalent circuit, CPE represents a constant phase element and is observed due to electrode/electrolyte interaction inhomogeneities due to the porosity, nature of the electrode, and disorder associated with diffusion.[50] It was confirmed that the R_{ct} of the Sb_2S_3/MoS_2 electrode (0.16 Ω cm^{-2}) was significantly lower than that of the Sb_2S_3 (4.15 Ω cm^{-2}) and MoS_2 electrode (0.31 Ω cm^{-2}). The excellent conductivity and large number of contact sites offered by the core Sb_2S_3 nanorods to clamp MoS_2 nanosheets were presumed to be responsible for the high number of uniformly distributed electroactive sites of MoS_2 nanosheets and facile ion diffusion. In addition, the straight line existing in the low-frequency region indicated the rapid diffusion of NH_4^+ ions and supported the idea that the core material could improve the electronic conductivity.

In addition, we investigated the CV performances of the Sb_2S_3/MoS_2 electrode at different scan rates in the range 5–100 mV s^{-1} (Fig. 2a). The nature of the CV curves indicated the pseudocapacitive nature and the current response increased linearly with the scan rate. The intensities of the curves indicated that the conversion reaction was entirely reversible, which may lead to a high capacity and coulombic efficiency. The kinetic behavior of the Sb_2S_3/MoS_2 electrode was further studied by fitting the power law relationship in the CV profile. Here, 'b' is defined as the slope of the plot of the log of the current against the log of the scan rate, and it has specified values like 0.5 and 1, which indicate that the charge-storage mechanism is either by diffusion control (0.5) or surface control (1).[51] The 'b' value plot for the Sb_2S_3/MoS_2 electrode is shown in Fig. S6d,† and its slope was 0.96, indicating that the electrode stored charges prominently through surface-controlled processes and that it exhibited considerable pseudocapacitive behavior.[52] The quantitative distribution of the charge-storage mechanism was further examined to evaluate the exact contribution from the surface and diffusion processes. The capacity contribution with the scan rate was calculated and is shown in Fig. 2b. At a 60 mV s^{-1} scan rate, the capacitive contribution percentage was 88% and the surface-controlled contribution increased with the increasing scan rate. The kinetic study results indicated that surface-controlled processes were mainly responsible for the charge storage in Sb_2S_3/MoS_2.

The GCD curves of the Sb_2S_3/MoS_2 electrode at current densities from 3–10 A g^{-1} displayed an almost symmetrical curve even at a low current density (3 A g^{-1}) (Fig. 2c) and the potential drop was significantly smaller than for the Sb_2S_3 electrode, demonstrating the low series resistance of the $Sb_2S_3/$

MoS_2 electrode. Fig. 2d shows the specific capacitance of the Sb_2S_3/MoS_2 electrode, extracted from the discharge profiles at various current densities. The electrode achieved a maximum gravimetric capacitance of 360 F g^{-1} at a current density of 3 A g^{-1}, demonstrating that the Sb_2S_3/MoS_2 heterostructure significantly improved the charge adsorption and increased NH_4^+ storage. This high capacitance improvement was mainly due to the enrichment of the MoS_2 surface activity. In addition, the long-term cycling stability of the Sb_2S_3/MoS_2 electrode was tested using GCD measurements at a current density of 12 A g^{-1} (Fig. 2e), revealing 90% of the specific capacitance of the Sb_2S_3/MoS_2 electrodes was retained after 5000 cycles and almost 97% of the corresponding coulombic efficiency during cycling. Moreover, the nature of the initial and final GCD cycles (Fig. S7†) corroborated the stable performance of the Sb_2S_3/MoS_2 electrode.

The excellent cycling stability of the electrode was due to its heterostructure, which prevented dissolution of the core due to the presence of surface oxygen (see the inset of Fig. 2e). It has been well demonstrated that H bonding between NH_4^+ and lattice O can stabilize lattice structures and suppress material dissolution.[53] Next, EIS measurements were performed to investigate the kinetics of the Sb_2S_3/MoS_2 electrode before and after cycling stability tests, and the Nyquist plots and the fitted circuit are provided in Fig. 2f. The small increment in R_{ct} observed after 5000 cycles indicated an increase in internal resistance;[54] the other parameters corresponding to the equivalent circuit are provided in Table S1.† The better electrode kinetics and electrochemical properties of the Sb_2S_3/MoS_2 electrode were presumably the result of the synergistic effects between the excellent conductivity of the Sb_2S_3 nanorods and the abundant electroactive sites provided by MoS_2 nanosheets that promote facile ion migration and storage. The above discussion reveals that the Sb_2S_3/MoS_2 is a promising anode candidate for NH_4^+ storage.

The well-reported MnO_2 was selected as a cathode for ammonium-ion storage due to its abundance, high theoretical capacitance, environment friendliness, and cost-effectiveness. A potentiodynamic method was used to synthesize free-standing MnO_2 electrodes on carbon cloth (CC), and deposition cycles were adjusted to achieve the optimum mass loading. XRD was used to investigate the structural features of MnO_2. The broad diffraction peaks around $2\theta = 30°$ and $43.6°$ were ascribed to the [002] and [100] planes of the carbon of the CC (Fig. S8a†), but no characteristic peaks of crystalline MnO_2 were observed. However, from the XPS study used to investigate the oxide nature of Mn, the survey spectrum confirmed the presence of Mn, O, and C (Fig. S8b†). The high-resolution Mn 2p spectrum is shown in Fig. S8c.† Two peaks could be observed at 654.3 and 642.1 eV, corresponding to the Mn 2p$_{1/2}$ and Mn 2p$_{3/2}$ states. After deconvolution, the peaks at 654.3 and 652.8 eV were assigned to Mn^{3+} and Mn^{4+} of Mn 2p$_{1/2}$,[55] and the peaks at 642.1 and 644.4 eV to Mn^{3+} and Mn^{4+} of Mn 2p$_{3/2}$.[55,56] The high-resolution O 1s spectrum (Fig. S8d†) showed two peaks at binding energies of 529.6 and 531.4 eV, representing lattice oxygen (Mn–O–Mn) and the presence of crystalline water,[20,57] which confirmed the formation of MnO_2 on the CC.
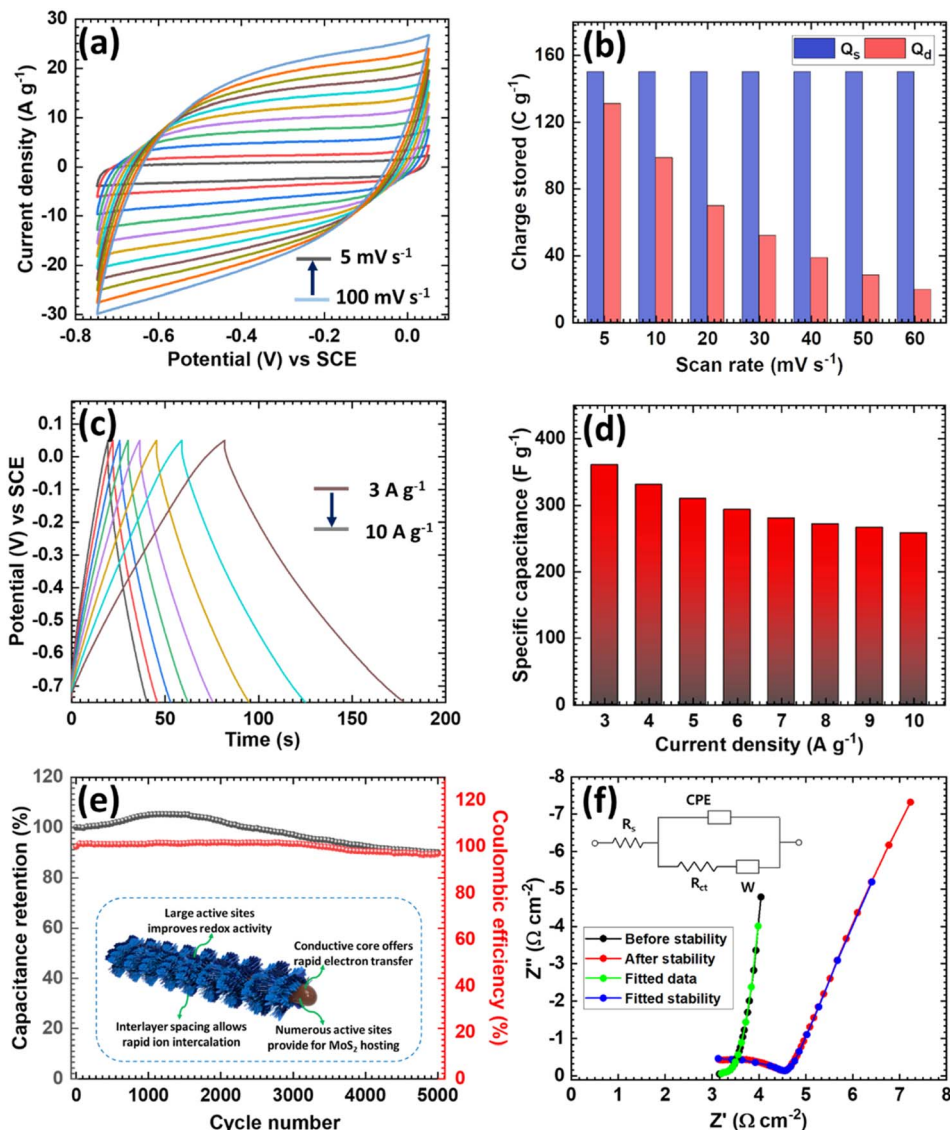
This journal is © The Royal Society of Chemistry 2024

J. Mater. Chem. A, 2024, **12**, 7587–7597 | **7591**

Fig. 2 Electrochemical study of heterostructured Sb_2S_3/MoS_2. (a) CV curves of Sb_2S_3/MoS_2, (b) surface and diffusive charges stored at different scan rates for Sb_2S_3/MoS_2, (c) GCD curves of Sb_2S_3/MoS_2, (d) specific capacitance of Sb_2S_3/MoS_2, (e) cycling stability of Sb_2S_3/MoS_2 and (f) Nyquist plots before and after Sb_2S_3/MoS_2 stability tests (inset: fitted circuit).

SEM and TEM were used to investigate the morphological and chemical compositions of the MnO_2 material. The microstructures of the synthesized Mn materials are presented in Fig. 3a, b and S9.† A single CC thread was used in the SEM study to investigate the morphological changes that occurred during cycling. The Mn-50 sample displayed fewer, more unevenly deposited particles on the CC (Fig. S9a†), and at higher magnification, a bundle of uniformly sized nanoparticles could be observed (Fig. S9b†) the other samples (Mn-100, Mn-150, and Mn-200) produced similar morphologies (Fig. S9c–f†). Upon increasing the number of deposition cycles, the MnO_2 loading on CC increased, and for the Mn-150 sample, a uniform coating of nanoparticles over the surface of CC was observed (Fig. 3a and b). The overgrowth of nanoparticles was observed for the Mn-200 sample. The TEM analysis (Fig. 3c and d) showed a similar morphology for the Mn-150 sample. Dense particles

could be observed in Fig. 3c and at higher magnification, the crystalline lattice fringes ($d = 0.27$ nm) were clearly marked (Fig. 3d and e), corresponding to the (400) plane of MnO_2 (JCPDS card no. 44-0141). The SAED pattern also verified the crystalline nature of MnO_2. Furthermore, EDX mapping of Mn-150 (Fig. 3f and S10†) showed the uniform distribution of Mn and O. These findings concurred with the XPS results and confirmed the successful deposition of MnO_2 on the CC.

The ammonium-ion-storage performances of a series of Mn electrodes were tested using half-cells in 1 M $(NH_4)_2SO_4$ electrolyte. Comparative CV curves at a constant scan rate (50 mV s^{-1}) and GCD curves at a current density of 3 A g^{-1} for the Mn series of electrodes measured in an optimized potential window of 0–1 V are shown in Fig. 3g and S11a.† The uniformly coated Mn-150 electrode delivered the highest current response in the CV study and the longest discharge time in the GCD study. A
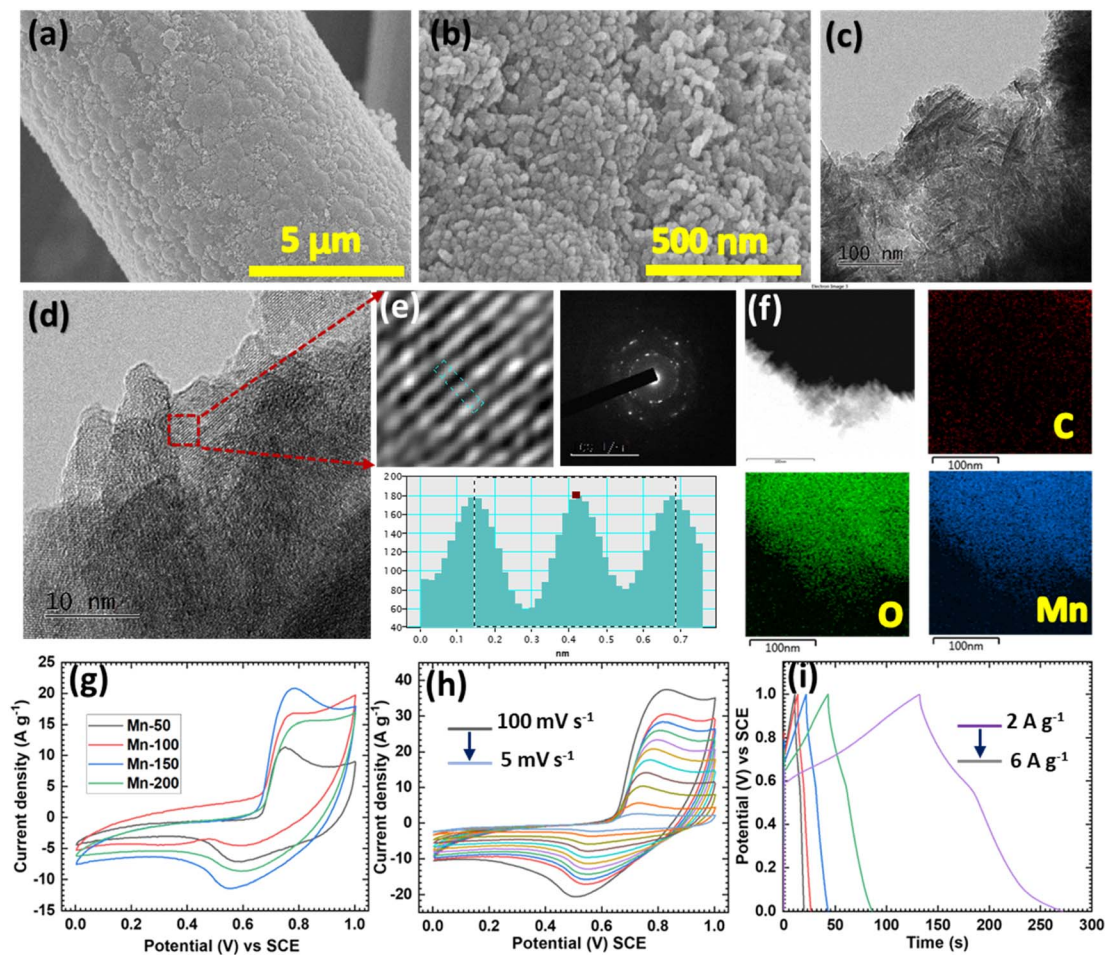
7592 | J. Mater. Chem. A, 2024, 12, 7587–7597

This journal is © The Royal Society of Chemistry 2024

Fig. 3 (a and b) SEM images of MnO_2 and (c–e) TEM images and (f) elemental mapping of MnO_2 (Mn-150 sample). (g) Comparative CV curves for the Mn series of electrodes. (h) CV curves at different scan rates and (i) GCD curves at different current densities for the Mn-150 electrode.

comparative study showed that the uniformly coated nanoparticles had higher NH_4^+-storage capacities than the uneven or overgrown nanoparticle structures (Fig. S10b†). Also, we investigated the scan rate and current density dependent analysis of the Mn-150 electrode (Fig. 3h and i). Upon increasing the scan rate, the current response of an electrode increased, and a minor shift occurred in the redox peaks due to the surface polarization of the charges.[58] In addition, the nature of the CV curves was well maintained over the scan rate study, suggesting the good reversibility of the Mn-150 electrode. Furthermore, at a lower current density of 2 A g^{-1}, the Mn-150 electrode delivered the highest specific capacitance of 278.6 F g^{-1} (Fig. S11c†). Nyquist plots of the Mn series of electrodes fitted with the equivalent circuit (Fig. S11d†) revealed that the Mn-150 electrodes had lower R_{ct} (98 Ω cm^{-2}) values than the other electrodes. Other parameters corresponding to the fitted circuit of the Mn series of electrodes are summarized in Table S2.† The above study shows that the electrodeposited MnO_2 cathodes are strong candidates for ammonium-ion capacitors.

The practical application of the developed materials was investigated by fabricating a full cell (AIHCs) by combining Sb_2S_3/MoS_2 as the anode and MnO_2 as the cathode. Here, the

charge balance theory was employed to balance the mass of the cathode and anode (1 : 0.96) and the obtained electrochemical performances are presented. A schematic presentation of the AIHC is illustrated in Fig. 4a. As shown in the figure, during the first charge, NH_4^+ ions are inserted in the Sb_2S_3/MoS_2 anode and extracted from the Sb_2S_3/MoS_2 during discharge. During the charge–discharge process, NH_4^+ ions are continuously shuttled between the anode and cathode.[16] The CV curves of the anode and cathode in different working potential windows at a constant scan rate are shown in Fig. 4b. A series of CV curves in different potential windows at a constant scan rate were used to define the optimum potential window for the AIHC, indicating 0–1.6 V was the optimum potential window for the AIHC (Fig. 4c). In addition, CV measurements of the AIHC at different scan rates (5–100 mV s^{-1}) obtained using the 0–1.6 V window (Fig. 4d) revealed a pair of reduction/oxidation peaks. At high scan rates, polarization shifted the positions of the oxidation and reduction peaks with the scan rates.[21] The symmetric nature of the CV curves suggested the excellent capacitor reversibility. The kinetics of the AIHC were investigated using the Power law, the relationship between the log of the current density and the log of the scan rate (Fig. S12a†).[59] Here, the 'b'
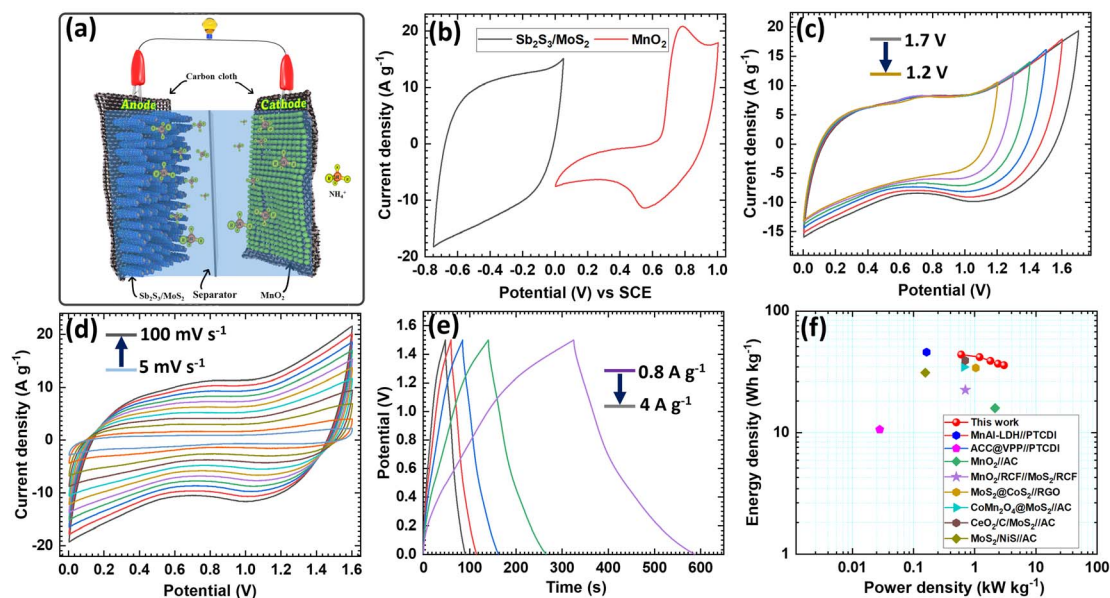
Fig. 4 Electrochemical study of AIHC. (a) Schematic presentation of ammonium-ion storage. (b) CV curves of MnO$_2$ and Sb$_2$S$_3$/MoS$_2$ in different voltage windows, (c) CV curves at different potential windows, (d) CV curves at various scan rates, (e) GCD curves at different current densities, and (f) Ragone plot comparison with materials reported in the available literature.

values of the cathodic and anodic peaks were accordingly 0.92 and 0.90, suggesting a combination of surface- and diffusion-controlled processes. These values indicate that the majority of the charges were contributed from the rapid reaction kinetics of a surface-controlled process.[60] The exact contributions from the surface- and diffusion-controlled processes were also calculated. Battery-type materials follow a slow charge-storage process due to the diffusion process while capacitive-type materials follow a fast charge-storage process due to the double-layer/surface charge-transfer process.[61,62] Here, the contribution from diffusive-(Q_d) and surface-controlled (Q_s) processes was calculated at different scan rates and estimated in Fig. S12b,† showing the contribution from the diffusion processes decreased with increasing the scan rate. Conversely, the charge contribution from the surface processes increased with increasing the scan rate from 53% (5 mV s^{-1}) to 89% (60 mV s^{-1}). Even at lower scan rates, the surface-controlled process still dominated the charge-transfer kinetics, which was favorable for high-rate performance and indicated that the Sb$_2$S$_3$/MoS$_2$ anodes are promising candidates for ammonium-ion capacitors.

GCD curves were also measured in different potential windows, and a symmetrical curve potential window was selected for further study (Fig. S12c†). The GCD performance was measured at various current densities, and symmetric curves were obtained without an IR drop (Fig. 4e). Specific capacitances were also extracted at different current densities from 0.8 to 4 A g^{-1}. The specific capacitances of the AIHC were 140, 133.4, 124.3, 117.6, and 114.5 F g^{-1} at 0.8, 1.2, 2.4, 3.2, and 4 A g^{-1}, respectively, with an excellent capacitive retention of 82% (Fig. S12d†). This suggests a high reversibility of NH$_4^+$ ion insertion/extraction and rapid kinetics at the cathode and

anode, which favor long-term cycle stability. The energy and power density of the AIHC were also determined to investigate the electrochemical features of the cell from the charge–discharge data (Fig. 4f). As can be seen in the Ragone plot, the AIHC delivered a maximum energy density of 43.75 W h kg^{-1} at a power density of 600 W kg^{-1}, which is comparable with those previously reported for AIHCs and supercapacitors.[9,15,20,63–67] In addition, a 5-fold increase in power density was observed; the AIHC achieved a power density of 3000 W kg^{-1} at an energy density of 35.77 W h kg^{-1}, indicating high reversibility and a rapid transmission of the charge carriers. Also, the long-term cycling performance of the AIHC was determined, because this is a crucial feature of energy-storage devices and is essential for commercial consideration. The cycling stability of the as-fabricated AIHC was examined at a 5 A g^{-1} current density (Fig. 5a). It was notable that the fabricated AIHC exhibited excellent cycle stability and retained almost 98.6% of its initial capacitance after 4000 cycles with 100% coulombic efficiency. The initial and final GCD cycles of the study are presented in the inset of Fig. 5a, which demonstrates the excellent retention and stability of the AIHC. In addition to its excellent cycle stability, the AIHC also showed an excellent rate capability (Fig. 5b). The specific capacitance of the AIHC was measured when the current density returned to a low current density of 0.8 A g^{-1} (140.8 F g^{-1}), which was almost identical to its initial value (140 F g^{-1}) at the same current density. Moreover, the AIHC maintained 100% coulombic efficiency at different current densities.

The reaction kinetics of the AIHC were investigated using the EIS technique. Nyquist plots of the AIHC before and after the cycling stability test are shown in Fig. 5c. The semicircles observed at high and intermediate frequencies corresponded to the solution resistance (R_s) and charge-transfer resistance (R_{ct}).

7594 | J. Mater. Chem. A, 2024, 12, 7587–7597

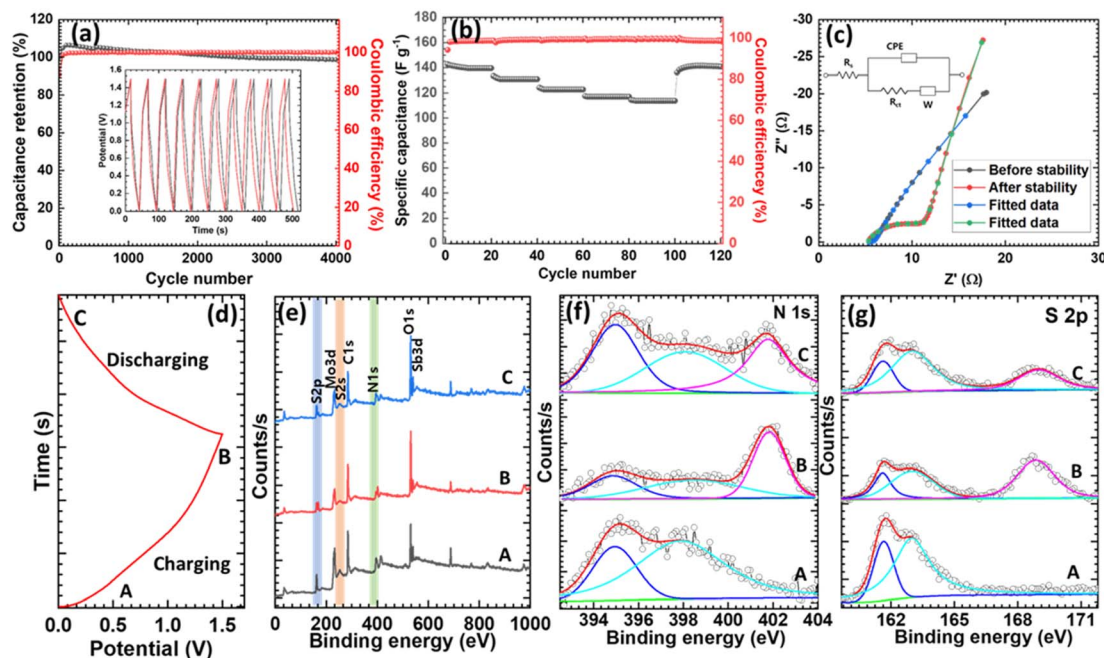This journal is © The Royal Society of Chemistry 2024

Fig. 5 (a) Cycling stability and (b) rate performance of the AIHC. (c) Nyquist plots before and after the cycling stability test of the AIHC with the fitted data (inset: fitted circuit). (d) Different charging/discharging state points on the GCD cycle. (e) *Ex situ* XPS survey spectra of the Sb_2S_3/MoS_2 electrode. *Ex situ* study of the high-resolution (f) N 1s and (g) S 2p spectra of the Sb_2S_3/MoS_2 electrode.

The straight line in the low-frequency region signified Warburg impedance related to the NH_4^+-diffusion kinetics in the active material. The AIHC showed a smaller R_{ct} (0.5 Ω), revealing its easy charge-transfer kinetics. In addition, after continuous cycling, the R_{ct} value increased slightly (5.6 Ω) due to negligible deterioration of the electrode structure.[68] Other parameters corresponding to the circuit are provided in Table S3.† The superior charge transfer and ion-diffusion kinetics of the AIHC were attributed to the highly conductive and porous structure of the electroactive material, which provides rapid electron pathways and allows easy electrolyte penetration and more easily accessible active sites for ammonium-ion storage.[68] These results suggest a new route toward the development of high-performance, stable ammonium-ion-storage systems for grid-scale applications.

Next, *ex situ* XPS characterizations were employed to study the structural evolution of the Sb_2S_3/MoS_2 material during NH_4^+ charging–discharging at different stages of the charge–discharge cycle, as shown in Fig. 5d. The full survey spectrum of the anode at various stages of charge–discharge is presented in Fig. 5e and confirmed the evolution in the S 2p and N 1s spectra. The high-resolution N 1s spectra of the anode at different states are shown in Fig. 5f. In the pristine state, the N 1s spectrum of Sb_2S_3/MoS_2 was deconvoluted into two peaks at 394.9 and 397.8 eV, associated with Mo 3p and –N–H–, respectively.[69–72] At fully charged, a new peak arose at 401.8 eV, ascribed to –N + H– segments, indicating the successful insertion of NH_4^+.[73] Furthermore, the –N–H– content was reduced and assigned to the protonation state (–N + H–) caused by the adsorption of NH_4^+ on the surface of the electrode.[19] After full discharge, the –

N + H– segment-associated peak intensity (401.7 eV) sharply decreased, indicating NH_4^+ extraction during discharge.[74] Furthermore, a new peak could be observed in Fig. 5g in the S 2p spectrum at 168.87 eV, corresponding to the oxidized sulfur remaining after discharge. This suggested that the sulfur was not totally returned to its original state and the inserted ions had not been completely extracted. In the high-resolution Mo 3d spectrum (Fig. S13a†), only a very slight shift in binding energy was observed in the fully charged state with a decreased intensity. In the fully discharged state, the peaks shifted toward the original state, confirming the insertion and extraction of NH_4^+ ions during the charge/discharge process. Similar results were observed in the high-resolution Sb 3d spectrum (Fig. S13b†), where the Sb 3d peaks were shifted toward higher binding energy on charging and returned to their original positions after discharging. In addition, the O 1s spectra were also examined (Fig. S13c†), and two deconvoluted peaks were observed, representing O from the core of the material (530.5 eV) and absorbed water (532.2 eV).[75] In the fully charged state, the intensity of the hydroxyl group increased, and the slight shift to higher energy indicated the insertion of NH_4^+ ions. After full discharge, the NH_4^+ ions were extracted, and the peaks re-emerged at their original energies. The existence of a peak at 401.7 eV after full discharge in the N 1s spectrum confirmed the insertion and presence of NH_4^+ ions in the electrode. The shifting and diminished intensities of the peaks in the elemental spectra that occurred upon charging also supported the insertion of NH_4^+ ions. These results disclosed that NH_4^+ ions were inserted and extracted from the Sb_2S_3/MoS_2 anode during charging and discharging.

This journal is © The Royal Society of Chemistry 2024

J. Mater. Chem. A, 2024, **12**, 7587–7597 | **7595**

The above results corroborate that the Sb_2S_3/MoS_2 anode is a promising candidate for ammonium-ion storage. The highly conductive Sb_2S_3 core helps to improve the conductivity of the heterostructured electrode material and effectively optimize the charge transport. The interlayer spacing of the MoS_2 shell material enables the easy insertion and extraction of ions, and improves the storage capacity of NH_4^+ ions. In addition, the heterostructure increases the specific surface area and provides highly active sites to interact with NH_4^+ ions. Furthermore, the presence of O increases the surface interactions, forms hydrogen bonds, and thus, increases the charge storage. This formation and breaking of bonds enables excellent NH_4^+ storage in the Sb_2S_3/MoS_2 electrode, while the interlayer spacing of the MoS_2 nanoshell increases the device storage capacity.

Conclusions

The use of non-metal charge carriers, especially ammonium ions, in electrochemical energy-storage devices has garnered attention because of their cost-effectiveness, safety, and environmentally friendly characteristics. We successfully developed a heterostructured Sb_2S_3/MoS_2 anode material using a two-step hydrothermal method. The heterostructure of the electrode improved the electrochemical performance due to the synergy between the nanorods and nanoflakes, facilitated easy ion transfer, and demonstrated a high specific capacitance of 360 F g^{-1}. In addition, an ammonium-ion hybrid capacitor constructed using a MnO_2 cathode and an Sb_2S_3/MoS_2 anode delivered superior energy and power density. Also, it exhibited excellent cycling performance, with a capacitive retention of 98.6% after 4000 cycles and a coulombic efficiency of 100%. In addition, *ex situ* XPS analysis was used to investigate the reversible insertion/extraction of NH_4^+ ions in the Sb_2S_3/MoS_2 anode during the charging and discharging process. This work demonstrates the potential of ammonium-ion hybrid capacitors and provides perspectives for the future anode materials required for ammonium-ion-storage systems.

Conflicts of interest

The authors declare no conflict of interest.

Acknowledgements

References

1 N. Yabuuchi, K. Kubota, M. Dahbi and S. Komaba, *Chem. Rev.*, 2014, **114**, 11636–11682.

2 M. T. F. Rodrigues, G. Babu, H. Gullapalli, K. Kalaga, F. N. Sayed, K. Kato, J. Joyner and P. M. Ajayan, *Nat. Energy*, 2017, **2**, 17108.

3 M. R. Lukatskaya, J. I. Feldblyum, D. G. Mackanic, F. Lissel, D. L. Michels, Y. Cui and Z. Bao, *Energy Environ. Sci.*, 2018, **11**, 2876–2883.

4 X. Wen, J. Luo, K. Xiang, W. Zhou, C. Zhang and H. Chen, *Chem. Eng. J.*, 2023, **458**, 141381.

5 F. Wang, O. Borodin, M. S. Ding, M. Gobet, J. Vatamanu, X. Fan, T. Gao, N. Edison, Y. Liang, W. Sun, S. Greenbaum, K. Xu and C. Wang, *Joule*, 2018, **2**, 927–937.

6 D. Chao and H. J. Fan, *Chem*, 2019, **5**, 1359–1361.

7 D. Chao, W. Zhou, F. Xie, C. Ye, H. Li, M. Jaroniec and S. Z. Qiao, *Sci. Adv.*, 2020, **6**, eaba4098.

8 Y. Ma, T. Sun, Q. Nian, S. Zheng, T. Ma, Q. Wang, H. Du and Z. Tao, *Nano Res.*, 2022, **15**, 2047–2051.

9 Q. Liu, F. Ye, K. Guan, Y. Yang, H. Dong, Y. Wu, Z. Tang and L. Hu, *Adv. Energy Mater.*, 2023, **13**, 1–11.

10 G. Liang, F. Mo, X. Ji and C. Zhi, *Nat. Rev. Mater.*, 2021, **6**, 109–123.

11 C. Lv, Y. Li, Y. Zhu, Y. Zhang, J. Kuang, Q. Zhao, Y. Tang and H. Wang, *Adv. Sci.*, 2023, **2304214**, 1–9.

12 Z. Guo, J. Huang, X. Dong, Y. Xia, L. Yan, Z. Wang and Y. Wang, *Nat. Commun.*, 2020, **11**, 959.

13 X. Zhang, G. Sun, S. Jia, H. Xie, Z. Kang, W. Chen, M. Cui, B. Wang, B. Wang, X. Chen and D. P. Yang, *Chem. Eng. J.*, 2022, **438**, 135624.

14 D. Yu, Z. Wei, X. Zhang, Y. Zeng, C. Wang, G. Chen, Z. X. Shen and F. Du, *Adv. Funct. Mater.*, 2021, **31**, 2008743.

15 X. Chen, P. Wang, Z. Feng, C. Meng and Y. Zhang, *Chem. Eng. J.*, 2022, **445**, 136747.

16 J. Han, A. Varzi and S. Passerini, *Angew. Chem.*, 2022, **134**, e202115046.

17 R. Slade and A. Roberts, *ECS Meet. Abstr.*, 2011, **MA2011-02**, 530.

18 Q. Chen, J. Jin, M. Song, X. Zhang, H. Li, J. Zhang, G. Hou, Y. Tang, L. Mai and L. Zhou, *Adv. Mater.*, 2022, **34**, 1–8.

19 T. H. Lu, C. Zeng, H. Zhang, X. Shi, Y. Yu and X. Lu, *Small*, 2023, **19**, 2206727.

20 S. G. Krishnan, H. D. Pham, C. Padwal, H. Weerathunga, X. Wang, K. Mahale and D. Dubal, *J. Power Sources*, 2023, **570**, 232994.

21 L. Yan, Y. e. Qi, X. Dong, Y. Wang and Y. Xia, *eScience*, 2021, **1**, 212–218.

22 Q. Chen, H. Li, X. Lou, J. Zhang, G. Hou, J. Lu and Y. Tang, *Adv. Funct. Mater.*, 2023, **33**, 2214920.

23 R. Zheng, Y. Li, H. Yu, X. Zhang, D. Yang, L. Yan, Y. Li, J. Shu and B. Su, *Angew. Chem.*, 2023, **135**, e202301629.

24 S. F. Kuchena and Y. Wang, *ACS Appl. Energy Mater.*, 2020, **3**, 11690–11698.

25 N. Murugan, S. Thangarasu, S. Bin Seo, Y. R. Choi, S. S. Magdum, T. H. Oh and Y. A. Kim, *Carbon Lett.*, 2023, **33**, 791–802.

26 Q. Li, Y. Zhang, Y. Song, H. Yang, L. Yang, L. Bai, D. Wei, W. Wang, Y. Liang and H. Chen, *Carbon Lett.*, 2023, **33**, 549–560.

27 X. Qin, J. Wan, Q. Zhang, Y. Zhang, H. Yu and S. Shi, *Carbon Lett.*, 2023, **33**, 781–790.

28 C. Wu, W. Xiong and H. Li, *Carbon Lett.*, 2023, **33**, 2327–2334.

7596 | *J. Mater. Chem. A*, 2024, **12**, 7587–7597

This journal is © The Royal Society of Chemistry 2024

29 N. W. Duffy, W. Baldsing and A. G. Pandolfo, *Electrochim. Acta*, 2008, **54**, 535–539.

30 K. Wang, Z. Wang, J. Liu, C. Li, F. Mao, H. Wu and Q. Zhang, *ACS Appl. Mater. Interfaces*, 2020, **12**, 47482–47489.

31 C. H. An, Y. Q. Li, S. Wu, L. X. Gao, L. Y. Lin, Q. B. Deng and N. Hu, *Rare Met.*, 2023, **42**, 1959–1968.

32 L. Wang, X. Zhang, C. Li, Y. Xu, Y. An, W. Liu, T. Hu, S. Yi, K. Wang, X. Sun, Y. Gong, Z. S. Wu and Y. Ma, *Chem. Eng. J.*, 2023, **468**, 143507.

33 T. Yan, F. Wen, J. Duan, C. Zhu, J. Wen, Y. Wang, J. Tong and Z. Chen, *Chem. Eng. J.*, 2023, **474**, 145839.

34 A. Panagiotopoulos, G. Nagaraju, S. Tagliaferri, C. Grotta, P. C. Sherrell, M. Sokolikova, G. Cheng, F. Iacoviello, K. Sharda and C. Mattevi, *J. Mater. Chem. A*, 2023, **11**, 16190–16200.

35 Y. Xiao, S. H. Lee and Y. K. Sun, *Adv. Energy Mater.*, 2017, **7**, 1601329.

36 K. Prakash, S. Harish, S. Kamalakannan, T. Logu, M. Shimomura, J. Archana and M. Navaneethan, *J. Energy Chem.*, 2023, **80**, 335–349.

37 W. Li, T. H. Ma, Y. Y. Dang, X. Y. Liu, J. Y. Li and C. Y. Wang, *Adv. Mater. Interfaces*, 2022, **9**, 2–9.

38 R. Jia, L. Li, G. Shen and D. Chen, *Sci. China Mater.*, 2022, **65**, 1443–1452.

39 C. Li, H. Song, C. Mao, H. Peng and G. Li, *J. Alloys Compd.*, 2019, **786**, 169–176.

40 Q. An, F. Lv, Q. Liu, C. Han, K. Zhao, J. Sheng, Q. Wei, M. Yan and L. Mai, *Nano Lett.*, 2014, **14**, 6250–6256.

41 G. Zhang, C. Zhou, J. Long, Y. Li, L. Lv, K. Yan, X. Chen, C. Dong, X. Xu and L. Mai, *Nano Res.*, 2023, **16**, 8488–8496.

42 W. He, C. Wang, H. Li, X. Deng, X. Xu and T. Zhai, *Adv. Energy Mater.*, 2017, **7**, 1700983.

43 X. Mu, Y. Song, Z. Qin, J. Meng, Z. Wang and X. X. Liu, *Chem. Eng. J.*, 2023, **453**, 139575.

44 Z. Zhang, J. Zhao, M. Xu, H. Wang, Y. Gong and J. Xu, *Nanotechnology*, 2018, **29**, 335401.

45 Z. Li, Y. Xu, X. Ren and W. Wang, *J. Mater. Sci.*, 2020, **55**, 13892–13904.

46 Y. Wang, M. Zhen and H. Liu, *J. Solid State Electrochem.*, 2018, **22**, 3069–3076.

47 L. Zou, R. Qu, H. Gao, X. Guan, X. Qi, C. Liu, Z. Zhang and X. Lei, *Results Phys.*, 2019, **14**, 102458.

48 Y. Yao, K. Ao, P. Lv and Q. Wei, *Nanomaterials*, 2019, **9**, 844.

49 B. Li, L. Jiang, X. Li, P. Ran, P. Zuo, A. Wang, L. Qu, Y. Zhao, Z. Cheng and Y. Lu, *Sci. Rep.*, 2017, **7**, 1–12.

50 J. Theerthagiri, K. Thiagarajan, B. Senthilkumar, Z. Khan, R. A. Senthil, P. Arunachalam, J. Madhavan and M. Ashokkumar, *ChemistrySelect*, 2017, **2**, 201–210.

51 C. Costentin, T. R. Porter and J. M. Savéant, *ACS Appl. Mater. Interfaces*, 2017, **9**, 8649–8658.

52 J. Wang, J. Polleux, J. Lim and B. Dunn, *J. Phys. Chem. C*, 2007, **111**, 14925–14931.

53 H. Zhang, Y. Tian, W. Wang, Z. Jian and W. Chen, *Angew. Chem.*, 2022, **134**, e202204351.

54 J. Dai, X. Qi, L. Xia, Q. Xue, L. Luo, X. Wang, C. Yang, D. Li, H. Xie, A. Cabot, L. Dai and Y. Xu, *Adv. Funct. Mater.*, 2023, **33**, 2212440.

55 Y. Z. Wu, Y. Ding, T. Hayat, A. Alsaedi and S. Y. Dai, *Appl. Surf. Sci.*, 2018, **459**, 430–437.

56 L. Yang, W. Zheng, J. Halim, J. Rosen, Z. M. Sun and M. W. Barsoum, *Batteries Supercaps*, 2023, **6**, e202200432.

57 M. Zhang, Y. Chen, D. Yang and J. Li, *J. Energy Storage*, 2020, **29**, 101363.

58 S. G. Krishnan, M. Harilal, B. Pal, I. I. Misnon, C. Karuppiah, C. C. Yang and R. Jose, *J. Electroanal. Chem.*, 2017, **805**, 126–132.

59 Y. An, Z. Li, Y. Sun, S. Li, Y. Xu, H. Dou and X. Zhang, *Batteries Supercaps*, 2022, **5**, e202200036.

60 S. Li, D. Yu, J. Liu, N. Chen, Z. Shen, G. Chen, S. Yao and F. Du, *Adv. Sci.*, 2023, **10**, 2206836.

61 M. Huang, X. Wang, X. Liu and L. Mai, *Adv. Mater.*, 2022, **34**, 1–33.

62 D. Li, S. Zhao, J. Li, Z. Yuan, J. Cao, X. Fu, Y. Zhang, L. Wang and W. Han, *Electrochim. Acta*, 2022, **411**, 140067.

63 C. Zhao, Y. Zhou, Z. Ge, C. Zhao and X. Qian, *Carbon*, 2018, **127**, 699–706.

64 Y. Li, H. Wang, T. Shu, J. Yuan, G. Lu, B. Lin, Z. Gao, F. Wei, C. Ma, J. Qi and Y. Sui, *J. Energy Storage*, 2022, **51**, 1–9.

65 R. Govindan, X. J. Hong, P. Sathishkumar, Y. P. Cai and F. L. Gu, *Electrochim. Acta*, 2020, **353**, 136502.

66 J. Hao, H. Liu, S. Han and J. Lian, *ACS Appl. Nano Mater.*, 2021, **4**, 1330–1339.

67 Q. Qin, L. Chen, T. Wei and X. Liu, *Small*, 2019, **15**, 1803639.

68 J. Yang, T. Wang, X. Guo and G. Wang, *Nano Res.*, 2023, **16**, 5592–5600.

69 Z. Yin, Y. Sun, C. Zhu, C. Li, X. Zhang and Y. Chen, *J. Mater. Chem. A*, 2017, **5**, 13648–13658.

70 J. Jia, M. Zhai, J. Lv, B. Zhao, H. Du and J. Zhu, *ACS Appl. Mater. Interfaces*, 2018, **10**, 30400–30408.

71 B. Chang, J. Yang, Y. Shao, L. Zhang, W. Fan, B. Huang, Y. Wu and X. Hao, *ChemSusChem*, 2018, **11**, 3198–3207.

72 S. H. Park, S. H. Kang and D. H. Youn, *Materials*, 2021, **14**, 1–10.

73 L. Xing, H. Chen, X. Wen, W. Zhou and K. Xiang, *J. Alloys Compd.*, 2022, **925**, 166652.

74 N. Lv, R. Ren, Y. Wu, Z. Xu, D. Wu, X. You, G. Zhu, Y. Zhang and S. Dong, *Electrochim. Acta*, 2022, **431**, 141097.

75 H. Idriss, *Surf. Sci.*, 2021, **712**, 121894.

This journal is © The Royal Society of Chemistry 2024

J. Mater. Chem. A, 2024, **12**, 7587–7597 | **7597**